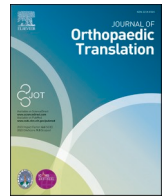




Contents lists available at ScienceDirect

Journal of Orthopaedic Translation

journal homepage: www.journals.elsevier.com/journal-of-orthopaedic-translation

Original article

Osteostaticytes: A novel osteoclast subset couples bone resorption and bone formation



Zhiyuan Wei^{a,1}, Jian Zhou^{b,1}, Jie Shen^a, Dong Sun^a, Tianbao Gao^b, Qin Liu^b, Hongri Wu^a, Xiaohua Wang^a, Shulin Wang^a, Shiyu Xiao^a, Chao Han^c, Di Yang^c, Hui Dong^c, Yuzhang Wu^c, Yi Zhang^d, Shuai Xu^e, Xian Wang^f, Jie Luo^g, Qijie Dai^a, Jun Zhu^h, Sien Lin^{i,**}, Fei Luo^{a,***}, Yi Tian^{c,****}, Zhao Xie^{a,*}

^a Department of Orthopedics, The First Affiliated Hospital of Third Military Medical University (Army Medical University), Chongqing, PR China

^b Biomedical Analysis Center, Third Military Medical University (Army Medical University), Chongqing, PR China

^c Institute of Immunology, PLA, Third Military Medical University (Army Medical University), Chongqing, PR China

^d Chongqing International Institute for Immunology, Chongqing, PR China

^e Department of Stomatology, The Second Affiliated Hospital of Third Military Medical University (Army Medical University), Chongqing, PR China

^f Department of Immunology, Medical College of Qingdao University, Qingdao, Shandong, PR China

^g Institute of Pathology and Southwest Cancer Center, The First Affiliated Hospital of Third Military Medical University (Army Medical University), Chongqing, PR China

^h Shanghai Intracore Biotechnology, Inc., People's Republic of China, Shanghai, PR China

ⁱ Musculoskeletal Research Laboratory, Department of Orthopaedics & Traumatology, Faculty of Medicine, The Chinese University of Hong Kong, Prince of Wales Hospital, Shatin, Hong Kong SAR, PR China

ARTICLE INFO

Keywords:

Bone
Bone remodelling
Osteostaticyte
Osteoclast
Reversal phase
scRNA-seq

ABSTRACT

Background: Osteomyelitis (OM) is an inflammatory condition of bone characterized by cortical bone devascularization and necrosis. Dysregulation of bone remodelling is triggered by OM. Bone remodelling is precisely coordinated by bone resorption and formation via a reversal phase. However, the cellular and molecular mechanisms underlying bone remodelling failure after osteomyelitis remain elusive.

Methods: To elucidate the cellular and molecular mechanism underlying bone healing after osteomyelitis, we employed single-cell RNA sequencing (scRNA-seq) to depict the atlas of human cortical bone in normal, infected and reconstructed states. Dimensionality reduction by t-stochastic neighbourhood embedding (t-SNE) and graph-based clustering were applied to analyse the detailed clusters of osteoclast lineages. After trajectory analysis of osteoclast lineages over pseudotime, real-time PCR and immunofluorescence (IF) staining were applied to identify marker gene expression of various osteoclast lineages in the osteoclast induction model and human bone sections, respectively. The potential function and communication of osteoclasts were analysed via gene set enrichment analysis (GSEA) and CellChat. The chemotactic ability of mesenchymal stem cells (MSCs) and osteoclast lineage cells in various differentiation states was determined by transwell assays and coculture assays. The effects of various osteoclast lineages on the osteogenic differentiation potential of MSCs were also determined by using this coculture system. A normal mouse tibia fracture model and an osteomyelitis-related tibia fracture model were generated via injection of luciferase-labelled *Staphylococcus aureus* to verify the relationships between a novel osteoclast lineage and MSCs. Then, the infection was detected by a bioluminescence imaging system. Finally, immunofluorescence staining was used to detect the expression of markers of MSCs and novel osteoclast lineages in different remodelling phases in normal and infected bone remodelling models.

Results: In this study, we constructed a cell atlas encompassing normal, infected, and reconstructed cortical bone. Then, we identified a novel subset at the earlier stage of the osteoclast lineage that exhibited increased expression of IDO1, CCL3, and CCL4. These IDO1^{high}CCL3^{high}CCL4^{high} cells, termed osteostaticytes (OSCs), were further

* Corresponding authors. Department of Orthopaedics, PLA, The First Affiliated Hospital of Third Military Medical University, Chongqing, 400038, PR China.

** Corresponding author.

*** Corresponding authors.

**** Corresponding author.

E-mail addresses: sienlin@cuhk.edu.hk (S. Lin), luofoespine@126.com (F. Luo), tianyi@tmmu.edu.cn (Y. Tian), xiezhaos4981@163.com (Z. Xie).

¹ Authors equally contributed to this article.

<https://doi.org/10.1016/j.jot.2024.06.010>

Received 4 January 2024; Received in revised form 4 June 2024; Accepted 11 June 2024

2214-031X/© 2024 Published by Elsevier B.V. on behalf of Chinese Speaking Orthopaedic Society. This is an open access article under the CC BY-NC-ND license (<http://creativecommons.org/licenses/by-nc-nd/4.0/>).

regarded as the reservoir of osteoclasts in the reversal phase. Notably, OSCs exhibited the highest chemotactic activity, surpassing other lineage subsets. We also discovered that cells at the earlier stage of the osteoclast lineage play a significant role in recruiting mesenchymal stem cells (MSCs). Finally, the data revealed that OSCs might be positively related to the occurrence of bone MSCs and the contribution of bone remodelling.

Conclusion: Collectively, our findings revealed a novel stage (OSC) within the osteoclast lineage, potentially representing elusive bone reversal cells due to its increased chemotactic ability towards MSCs and potential contribution to bone remodelling. This study provides valuable insights into the intricate mechanisms of the reversal phase during bone remodelling and unveils potential therapeutic strategies for diseases associated with bone uncoupling.

Translational potential of this article: This study identified a new subset, referred to as IDO1(plus symbol) CCL3 (plus symbol) CCL4(plus symbol) osteostaticytes which displayed the highest chemotactic activity among all osteoclast lineages and may serve as reversal cells in bone remodelling. These findings offer new insights and insights for understanding bone reversal-related diseases and may serve as novel therapeutic targets for conditions such as osteomyelitis and delayed bone healing.

Translational potential of this article: This study identified a new subset, referred to as IDO1⁺ CCL3⁺ CCL4⁺ osteostaticytes which displayed the highest chemotactic activity among all osteoclast lineages and may serve as reversal cells in bone remodelling. These findings offer new insights and insights for understanding bone reversal-related diseases and may serve as novel therapeutic targets for conditions such as osteomyelitis and delayed bone healing.

1. Introduction

Bone is a dynamic organ that is constantly constructed and reconstructed throughout human life in response to different environmental stimuli through two processes: bone modelling and remodelling [1]. Typically, bone remodelling is perceived as a process comprising five progressive stages that unfold in a synchronized and sequential manner. These stages include activation, resorption, reversal, formation, and termination. Osteoclastic bone resorption and osteoblastic bone formation are the major phases of bone remodelling and are tightly coupled both spatially and temporally; this process is termed bone reversal [2]. Observations suggesting uncoupling and bone loss have been repeatedly reported in diverse situations, such as ageing [3], unloading [4], periodontitis [5] and glucocorticoid- and menopause-induced osteoporosis [6,7]. Thus, it is necessary to investigate the chain of events occurring after the initiation of resorption and before the initiation of formation within basic multicellular units (BMUs) by constructing a balanced or unbalanced bone remodelling model.

Osteomyelitis (OM) is an infectious disease characterized by unbalanced bone remodelling resulting from an infection that poses a significant threat to human health and has high potential for causing disability. Antibiotic treatment cannot effectively eliminate the infection. Surgical debridement is routine for these patients, but the recurrence rate and reoperation rate are still high due to the difficulty in discriminating the severity of infection. The main pathophysiological change in OM is an inflammatory state of bone, in which bone devascularization and necrosis of cortical bone are the predominant features. Moreover, systemic dysregulation of bone homeostasis, including unbalanced bone remodelling, impaired vascular construction, and a protective host immune response, is triggered by OM. Previous studies have reported that distinct cell types are involved in changes in bone homeostasis during OM. However, the cell atlas and molecular mechanism underlying bone healing after osteomyelitis remain elusive.

The reversal phase is defined as a linking stage that temporally and spatially couples bone remodelling via the recruitment and differentiation of bone marrow mesenchymal stem cells (MSCs) for subsequent formation [8]. However, the nature of bone reversal remains controversial. In the late 1970s, Roland Baron et al. primarily defined these reversal cells as large mononucleated cells [9]. However, recent studies have reported that the reversal cell is from the osteoblast lineage, based on cell morphology, positive expression of alkaline phosphatase (ALP) and the absence of the monocyte/macrophage marker monocyte +

macrophage antibody-2 (MOMA-2) [10]. Notably, studies also reported that other macrophage clusters could express ALP and MOMA-2 [11]. In addition, Delaisse et al. showed that mononucleated reversal cells were of the osteoblast lineage and were packed with sparse numbers of TRAcP- and CatK-positive cells on the resorbed surface of cortical bone [10]. The reversal phase is short-lived, and it is difficult to continuously observe reversal phases in vivo. However, until recently, our understanding of the cellular and molecular events that occur during reversal has remained elusive. More recently, single-cell RNA sequencing (scRNA-seq) has been able to provide molecular definitions and predict potential cell functions or unveil the underlying cellular communication of biological processes [12].

Therefore, in this study, we performed scRNA-seq on three different bone remodelling states, namely, normal cortical bone, infected cortical bone, and reconstructed cortical bone, to simultaneously observe the biological features of osteoclast lineage cells in different remodelling states. Surprisingly, we identified a novel cell set at an earlier stage during the osteoclastogenic lineage, named the osteostaticyte (OSC), which differs from other subsets exhibiting greater chemotactic ability towards MSCs. To further investigate the biological functions of osteoclast lineages during different bone remodelling processes, we performed MSCs coculture on osteoclast induction progression and determined that the chemotaxis ability of mononuclear osteoclast lineage cells towards mesenchymal stem cells showed a trend of first increasing and then decreasing. Interestingly, the osteogenic effect of osteoclast lineage cells on MSCs gradually increases. Mouse fracture models revealed that OSCs might be positively related to the occurrence of bone MSCs and bone remodelling. Collectively, our findings lay a solid foundation for the use of OSCs as reversal cells in bone remodelling, which offers new therapeutic strategies to improve uncoupling-related bone diseases.

1.1. Methods and materials

Cell culture. Mouse bone marrow mesenchymal stem cells (BMSCs) were obtained from Procell Life Science & Technology Co., Ltd. (Wuhan, China) and grown in DMEM (Gibco, Carlsbad, California, United States). The media used in this study contained 10 % foetal bovine serum (FBS; Gibco) and 1 % antibiotics. The cells were cultured in a humidified environment with 5 % CO₂ at 37 °C. Mouse bone marrow mononuclear cells were isolated from the hind limbs of 11-week-old male C57BL/6 mice (femur and tibia) and incubated with macrophage colony-stimulating factor (M-CSF, 50 ng/ml, R&D Systems, Minneapolis, MN, USA) for 48 h to obtain bone marrow-derived macrophages (BMMs). To induce osteoclasts, adherent monocytes were incubated with M-CSF (50 ng/ml) and RANKL (50 ng/ml, R&D Systems, Minneapolis, MN, USA) or Staphylococcal Protein A (SPA) (20 ng/mL, USCN, Wuhan, China) for 6 consecutive days, and the medium was changed every other day.

Transwell assay and ALP staining. The chemotactic ability of osteoclast lineages was assessed by transwell assays, which were carried

out with 24-well Transwell plates (8- μ m pore size; Millipore, Bedford, Massachusetts, United States); 1×10^5 MSCs were seeded in the upper chamber, whereas 1×10^5 cells of the osteoclast lineage from days 1, 2, 3, 4, 5 or 6 were seeded in the lower chamber during osteoclast induction. The cells were cultured in osteoclast induction medium. After incubation for 24 h, the cells on the bottom surface of the filter were fixed with 4 % paraformaldehyde, stained with haematoxylin-eosin dye, and counted. To identify the crucial chemokines of OSCs, 0.5 μ M maraviroc (MCE, USA) was added to the medium. The impact of osteoclast lineages on the osteogenic differentiation of MSCs was assessed by cell–cell coculture with a 0.4- μ m pore size chamber. A total of 1×10^5 cells of osteoclast lineage from days 1, 2, 3, 4, 5 or 6 during osteoclast induction were seeded in the upper chamber, whereas 1×10^5 MSCs were seeded in the lower chamber. The cells were cultured in osteogenic induction medium for 24 h, after which the chambers were removed. After culture for another 4 days, the cells on the bottom surface of the filter were fixed with 4 % paraformaldehyde and stained with ALP, and the replicate wells were tested. ALP assays were performed using an alkaline phosphatase assay kit (Beyotime, Shanghai, China).

Bone resorption assay For the bone resorption assay, cells were cultured on Osteo Assay Surface plates (3988; Corning). Cells were seeded in plates according to the osteoclast induction protocol. Photographs were taken on days 3 and 6 of induction to compare the absorption of inorganic calcium phosphate on the bone plates. After the plates were washed with deionized water and completely air-dried, bone resorption pits were observed by using a light microscope, and resorption areas were evaluated by ImageJ software.

Participants and clinical material collection. Five specimens were collected from 4 patients who were prospectively enrolled in this study and hospitalized from August 2020 to November 2021 at the Army Medical University First Affiliated Hospital; the study was approved by the Army Medical University First Affiliated Hospital Ethics Committee ((A)KY2021084). Patient care and research were conducted in accordance with the Care Guidelines and Declaration of Helsinki. Samples for scRNA-seq were derived from the cortical tibia or femur sites of four patients who had received debridement for primary OM and second-stage tibial internal fixation and removal via surgery. The clinical data of the patients, including case information, X-ray, radionuclide bone imaging and MRI, were collected from the Army Medical University First Affiliated Hospital (SM, Table 1).

Sample preparation and cell isolation for scRNA-seq. Fresh normal, infected or reconstructed cortical bone tissue was obtained by bone nipper or chisel surgery, stored in tissue preservation solution (CapitalBio Technology, China) and transported in an ice box with real-time temperature surveillance within 4 h. Then, the specimens were washed with 0.9 % NaCl balanced salt solution three times and further minced into 0.2 cm bone fragments with a rongeur on a sterile operation platform. The bone tissue was digested in 0.25 % trypsin solution (Gibco) at 37 °C for 5–10 min. Next, the trypsin was discarded, and the

cells were washed once with balanced salt solution. The bone tissue was transferred to a 15 ml centrifuge tube, and then, the tissue digestive solution (CapitalBio Technology, China), which contained collagenase II, calcium chloride, foetal bovine serum and 1640 medium, was added, and digestion was performed at 37 °C for 14 h. After digestion, the samples were filtered through 40- μ m sterile strainers and centrifuged at 1500 \times g for 5 min. Subsequently, the supernatants were discarded, and the cell pellets were suspended in 1 mL of phosphate-buffered saline (PBS; Biotime, China). To remove red blood cells, 2 mL of red blood cell lysis buffer was added, and the cells were incubated at 25 °C for 10 min. The solution was then centrifuged at 800 \times g for 5 min and resuspended in PBS. The samples were stained with trypan blue (Sigma, United States), and the cellular viability was evaluated under a phase contrast light microscope (Nikon, Japan).

Quantitative real-time PCR (qRT-PCR). Total cell RNA was extracted with TRIzol reagent (Invitrogen) according to the manufacturer's recommendations. Two hundred nanograms of RNA was used to synthesize first-strand cDNA using a PrimeScript RT Kit (Takara, Dalian, China). Quantitative real-time PCR was performed using TB Green Premix Ex Taq (Takara) following the manufacturer's protocol. The indicated gene expression was normalized to GAPDH expression by the $2^{-\Delta\Delta Ct}$ method. The primers used are listed in the SM, Table 2.

Single-cell RNA sequencing, cell capture and cDNA synthesis. Using the Single Cell 3' Library and Gel Bead Kit V3 (10x Genomics, 1000075) and Chromium Single Cell B Chip Kit (10x Genomics, 1000074), the cell suspension (300–600 living cells per microlitre, as determined by Count Star) was loaded onto a Chromium single-cell controller (10x Genomics) to generate single-cell gel beads in the emulsion according to the manufacturer's protocol. Briefly, single cells were suspended in PBS containing 0.04 % BSA. Approximately 10,000 cells were added to each channel, and the target cell recovery was estimated to be approximately 7000 cells. The captured cells were lysed, and the released RNA was barcoded through reverse transcription in individual GEMs. Reverse transcription was performed on an S1000TM Touch Thermal Cycler (Bio-Rad) by heating at 53 °C for 45 min, followed by heating at 85 °C for 5 min and then holding at 4 °C. cDNA was generated and then amplified, and the quality was assessed using an Agilent 4200 (performed by CapitalBio Technology, Beijing). Single-cell RNA-Seq library preparation was performed according to the manufacturer's instructions for the Single Cell 3' Library and Gel Bead Kit V3. The libraries were finally sequenced using an Illumina NovaSeq 6000 sequencer with a sequencing depth of at least 100,000 reads per cell with a paired-end 150-bp (PE150) reading strategy (performed by CapitalBio Technology, Beijing).

1.2. Single-cell gene expression quantification and subcluster detection

CellRanger pipeline. Cell Ranger software was obtained from the 10x Genomics website (<https://support.10xgenomics.com/single-cell-gene-expression/software/downloads/latest>.) Alignment, filtering, barcode counting, and UMI counting were performed with the cellranger count module to generate a feature-barcode matrix and determine clusters. Dimensionality reduction was performed using PCA, and the first ten principal components were used to generate clusters via the K-means algorithm and a graph-based algorithm.

Seurat pipeline. Raw gene expression matrices were imported and processed using the Seurat R package (version 4.0) [13]. Low-quality cells were removed following two measurements: 1) cells that had fewer than 200 unique molecular identifiers (UMIs), more than 6000 or less than 500 expressed genes, or more than 20 % UMIs derived from the mitochondrial genome; and 2) cells that had an average expression level of less than 2 for a curated list of housekeeping genes. The gene expression matrices of the remaining high-quality cells were normalized to the total cellular UMI counts. The normalized expression was scaled (scale factor = 1e4) by regressing out the total cellular UMI counts and percentage of mitochondrial genes. Highly variable genes were

Table 1
q-PCR primers.

Gene names	Primers (5'-3')
Ccl3	Forward: TTCTCTGTACCATGACACTCTGC Reverse: CGTGAATCTTCCGGCTGTAG
Ccl4	Forward: TTCTGTCTGTTTCTCTTACACCT Reverse: CTGTCTGCCTCTTTTGGTCAG
F4/80	Forward: TGACTCACCTTGTGGTGCTAA Reverse: CTTCCAGAAATCCAGTCTTCC
Ido1	Forward: GCTTTGCTCTACACATCCAC Reverse: CAGGCGCTGTAACCTGTGT
Ctsk	Forward: GAAGAAGACTCACCAGAAGCAG Reverse: TCCAGGTTATGGGCAGAGATT
Acp5	Forward: CACTCCCACCCTGAGATTTGT Reverse: CATCGTCTGCACGGTTCTG
Hprt	Forward: TCAGTCAACGGGGGACATAAA Reverse: GGGGCTGTACTGCTTAACCAG

identified using the Seurat FindVariableGenes function with default parameters except for “x.low.cut-off” = 0.0125 and y.cut-off = 0.5. Then, we performed PCA using the highly variable genes, and significant PCs (top 100) were selected to perform dimension reduction. Clusters were found using the FindClusters function (dims.use = 1:50, resolution = 0.2). tSNE analysis was used for dimension reduction and visualization of gene expression [14].

Enrichment analysis To identify biological functions associated with each cluster, we performed GO and KEGG enrichment analyses on the top 100 genes specifically expressed in each cell population using the clusterProfiler package. The top 3 pathways with p values < 0.05 were selected, and ggplot2 was used for histogram plotting. The results were visualized using the R package.

Cell type annotation Unbiased cell type recognition from single-cell RNA sequencing data was performed by leveraging reference transcriptomic datasets of pure cell types to infer the cell of origin of each single cell independently. For humans, Blueprint Encode or HPCA was used. Highly variable genes were identified as those with a normalized expression between 0.125 and 3 as well as quantile-normalized variance exceeding 0.5. Thereafter, PCA was used to reduce the number of dimensions representing each cell. We adopted the first 20 principal components to further conduct tSNE dimensionality reduction using the default settings of the Run tSNE function. Cell types in the resulting two-dimensional representation were annotated to known biological cell types using canonical marker genes and the putative CNV signal.

Osteostaticyte induction assay. For osteostaticyte induction, according to our trajectory results, we hypothesis that OSC is lying in the differentiation process of monocytic osteoclast. Mouse bone marrow macrophage (BMM) were flushed from 8 to 10 weeks C57BL/6 mouse femoral bone marrow cavity and then incubated in 24-well plates at a density of 1×10^5 cells per well with M-CSF (50 ng/mL) for the former 3 days. Then the cells were co-stimulated with M-CSF (50 ng/mL) and RANKL (50 ng/mL). Cells were collected as the schematic showed. Total cell RNA was extracted by TRIzol reagent (Invitrogen) according to the manufacturer’s recommendations.

Trajectory analysis of single cells. The single-cell pseudotime trajectories were generated with the Monocle2 package (v2.8.0) in R [15]. The gene-cell matrix at the scale of the raw UMI counts derived from the Seurat processed data was used as the input. The new-CellDataSet function was applied to create an object with the parameter expressionFamily = negbinomial.size. Only genes with a mean expression ≥ 0.1 were used in the trajectory analysis. DEGs with q-values < 0.01 between the cell groups were subjected to dimension reduction, and the reduceDimension function was used with the parameters reduction_method = “DDRTree” and max_components = 2. The cells were ordered and visualized with the plot_cell_trajectory function. Genes that changed with pseudotime were identified (q-val $< 10^{-10}$) and visualized with plot_pseudotime_heatmap, and the genes were clustered into subgroups according to their gene expression patterns.

Gene Set Enrichment Analysis. Gene set enrichment analysis (GSEA) was performed using GSEA software (<https://www.broadinstitute.org/gsea/>). The R package (junjunlab/GseaVis <https://github.com/junjunlab/GseaVis>) was used to visualize the GSEA enrichment results.

Cell–Cell Communications CellChat 1.1.0 (<https://github.com/sqjin/CellChat>) was used for the analysis of cell-to-cell communication in each sample. First, LMC-derived cells were subsetted from the total cell population and annotated according to their cell type: “OSC”, “macrophage”, “pre-OC”, “osteoclast” (OC), “osteomorph”, “osteocyte”, “MSC.adipo”, “osteoblast” and “MSC_osteo” cells. The CellChat model was constructed using the “createCellChat” function. After annotating the object with relevant labels and identifying overexpressed genes, the communication probability was inferred using the “computeCommunProb” function. Cell–cell communications for each cell signalling pathway were generated with the “computeCommunProbPathway” function. Graphs were generated using the “netVisual_chord_gene”

function.

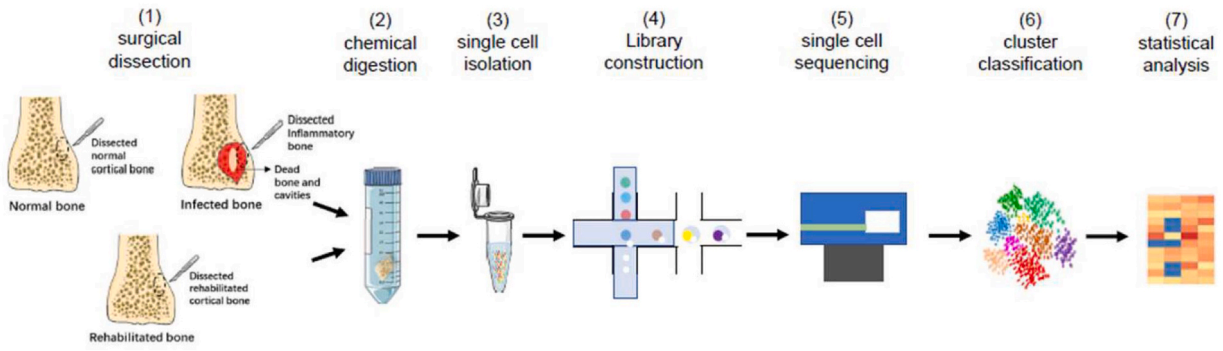
Mouse fracture model. Eight-to ten-week-old C57BL/6 mice were purchased from the Laboratory Animal Centre of Third Military Medical University (Chongqing, China). All mice were bred under SPF conditions in the Laboratory Animals Center of Army Medical University (Third Military Medical University, Chongqing, China). Age- and sex-matched littermates were used as control mice. All experiments were conducted according to the Third Military Medical University Sciences Guide for Laboratory Animals. Eight-week-old male or female mice were used for the model. The mice were anaesthetized using 0.5 % sodium pentobarbital (P3761, Sigma–Aldrich). A closed, transverse fracture was induced in the tibia through the three-point bending method: two tweezers were used to clamp the mouse’s lower limb at positions 1 mm on each side of the tibia-fibula junction, and then the located area was pressed against a triangular pyramid. The standard for bending is to feel a sense of bone fracture. Postoperatively, we used imaging to confirm the fracture.

Bioluminescence imaging of *Staphylococcus aureus* in the mouse tibia infection model. C57BL/6 mice (n = 4 for each group) were fully anaesthetized with 1 % (m/v) pentobarbital sodium (50 mg/kg). A mixture containing 2 μ L of 1×10^5 CFU of *S. aureus* USA300/Eno-Antares2 and 50 μ L of hydrofurimazine (HFZ) (100 μ M) was injected into the fractured lesion of a mouse. BL signals were measured every four days using the IVIS® Lumina LT system.

Micro-CT analysis. Mice were anaesthetized using 0.5 % sodium pentobarbital and then scanned using a Bruker micro-CT SkyScan 1276 system (Kontich, Belgium). At the indicated endpoints, the mice were euthanized, and their lower limbs were collected, fixed with 4 % paraformaldehyde for 24 h and then scanned using the MicroCT system at a high resolution. The main parameters used during microCT scanning were as follows: source voltage (Kv) = 50, source current (μ A) = 200, exposure (ms) = 684, and filter = Al 0.25 mm. NRecon v1.6 software (Bioz, Inc., United States) was used to reconstruct the scanned image. The reconstruction was analysed using CTAn v1.9 software (Bruker micro-CT), and CTVol v2.0 software (Bruker micro-CT) was used to visualize the 3D model (SM. Fig. 1). All the calluses in the fracture area, as the area of interest (ROI), were defined according to the “fracture callus analysis” section of the Bruker micro-CT method annotation as follows: The entire outer boundary of both normal bone (high-density) and callus (low-density) was identified, and the entire callus was defined as the ROI by subtracting the boundary of the normal bone (SM. Fig. 1A and B). After selecting the ROI, we further calculated the density within this ROI and performed a morphological analysis of the ROI after binarizing the image (SM. Fig. 1C and D).

Tartrate-resistant acid phosphatase (TRAP) staining, safranin O/fast green staining and haematoxylin–eosin (H&E) staining For TRAP staining, TRAP activity was detected in the paraffin sections using a TRAP staining kit (SLBT1113, Sigma, USA) according to the manufacturer’s instructions. For Safranin O/fast Green staining, the slices were stained with 0.1 % Safranin O solution and 0.1 % Fast Green solution. H&E staining was performed, including dewaxing, immersion, staining, differentiation, blue promotion, dehydration, transparency, etc. To quantify TRAP staining, we randomly selected five fields at a magnification of $400 \times$, counted the number of TRAP-positive cells (No. OC), and calculated the trabecular bone volume (BV) via ImageJ software. The number of TRAP-positive cells per unit area was determined by the number of OCs/BV. For quantification of safranin-O and fast green staining, we randomly selected five $400 \times$ high-power fields. The blue area of each field was considered the trabecular bone volume and was calculated via ImageJ. The whole field of each image was considered the total bone volume (TV). BV/TV was calculated from these two values. For quantification of HE staining, we randomly selected five fields at a magnification of $400 \times$ and counted the number of osteoblasts (No. OB) through morphological identification. Moreover, the trabecular bone volume was measured via ImageJ software. Then, the number of osteoblasts per unit of trabecular bone area was determined by the

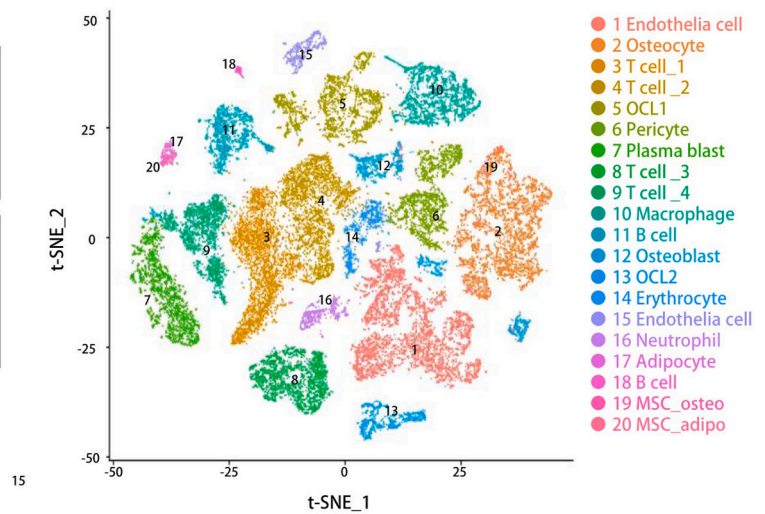
A



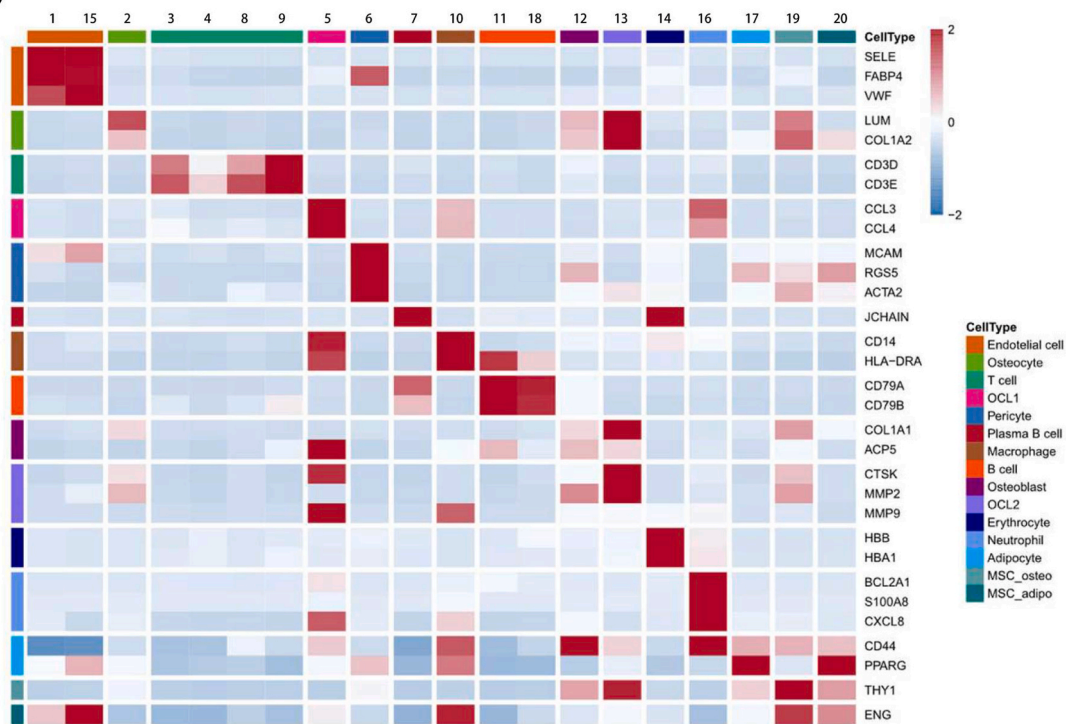
B



C



D



(caption on next page)

Figure 1. Cell atlas among normal, infected, and reconstructed cortical bone tissues **A)** Schematic workflow of the experimental strategy. Single-cell suspensions were collected from the lesions of patients with normal long bone fracture, patients with osteomyelitis and patients subjected to removal of internal fixation after bone reconstruction. **B)** Representative preoperative radiographs of patients with lesions, including X-ray, radionuclide bone imaging and MRI. **C)** The t-distributed stochastic neighbour embedding (t-SNE) plot of the 18 identified main cell types in human cortical bone lesions. **D)** Heatmap of selected lineage cell marker genes in each cell cluster. Relative expression map of known marker genes associated with each cell subset. Mean expression values were scaled by mean centering and transformed to a scale from -2 to 2 . **E)** The t-SNE plot divided by 3 distinct sample states (normal bone, infected bone, and reconstructed bone) depicting all identified main cell types in human cortical bone lesions. **F)** Histogram depicting the proportion of cells from different sample sources in each cell cluster. **G)** Histogram depicting the relative proportion of each cell cluster among the respective sample states in all cortical bone lesions as indicated. The values of the detailed relative proportion of each cell cluster are provided in the supplementary data file.

number of OBs/BV.

Immunofluorescence (IF) assay. Bone tissues were collected from clinical surgery were the same as scRNA samples (SM. Table 2). Then tissues were fixed in 4 % paraformaldehyde for 48 h. The cortical bone tissue was decalcified with 10 % EDTA decalcifying solution every other day for 50–60 days. The tibia of mice is only decalcified for one week with 0.5M EDTA decalcification. Then, through dehydration, embedding and sectioning, the decalcified bone tissue is made into paraffin sections. The blocks were sectioned at 4 μm or 10 μm (for immunofluorescent staining) intervals using a Paraffin Microtome (for paraffin blocks). We incubated the slides at 37 °C for 30 min and washed the sections three times with PBS. The sections were incubated with a blocking solution for 1 h and then with primary antibodies to human CD14 (sc-58951, 1:100, Santa Cruz Biotechnology Inc.), human MIP-1a (CCL3, sc-166942, 1:50, Santa Cruz Biotechnology Inc.), human IDO1 (sc-53978, 1:50, Santa Cruz Biotechnology Inc.) overnight at 4 °C in a humidified chamber, followed by incubation for 1 h at room temperature. The sections were washed three times with Tris-buffered saline. We then used secondary antibodies conjugated with fluorescence at room temperature for 1 h while avoiding light. The sections were mounted in ProLong Gold Mounting Reagent with DAPI (P36935, Life Technologies). We used isotype-matched controls under the same concentrations and conditions as the negative controls.

For mouse tibia sections, paraffin sections were stained four-color-multilabeled immunofluorescence staining kit (Absin, abs50012) according to the manufacture's protocols. Antibodies used include rabbit anti-CD90 (1:500 dilution, Proteintech, 27178-1-AP), and rabbit anti-IDO1(1:500 dilution, Proteintech, A1614). Immunofluorescence imaging was performed using an LSM 710 inverted confocal microscope (Zeiss). CD14 is considered a surface marker of monocytes and macrophages. MIP-1a and IDO1 are considered cell markers of osteostaticytes. And CD90 is the canonical surface of MSCs.

Quantification and statistical analysis. Data are presented as mean \pm SD. The differences between two groups were determined by two-sided, unpaired Student's t-test. p values smaller than 0.05 are considered significant. For in vivo experiments, all p values are spelled out. Sample size for all animal experiments was between 3 and 5 per group while all in vitro experiments were repeated at least three times.

2. Results

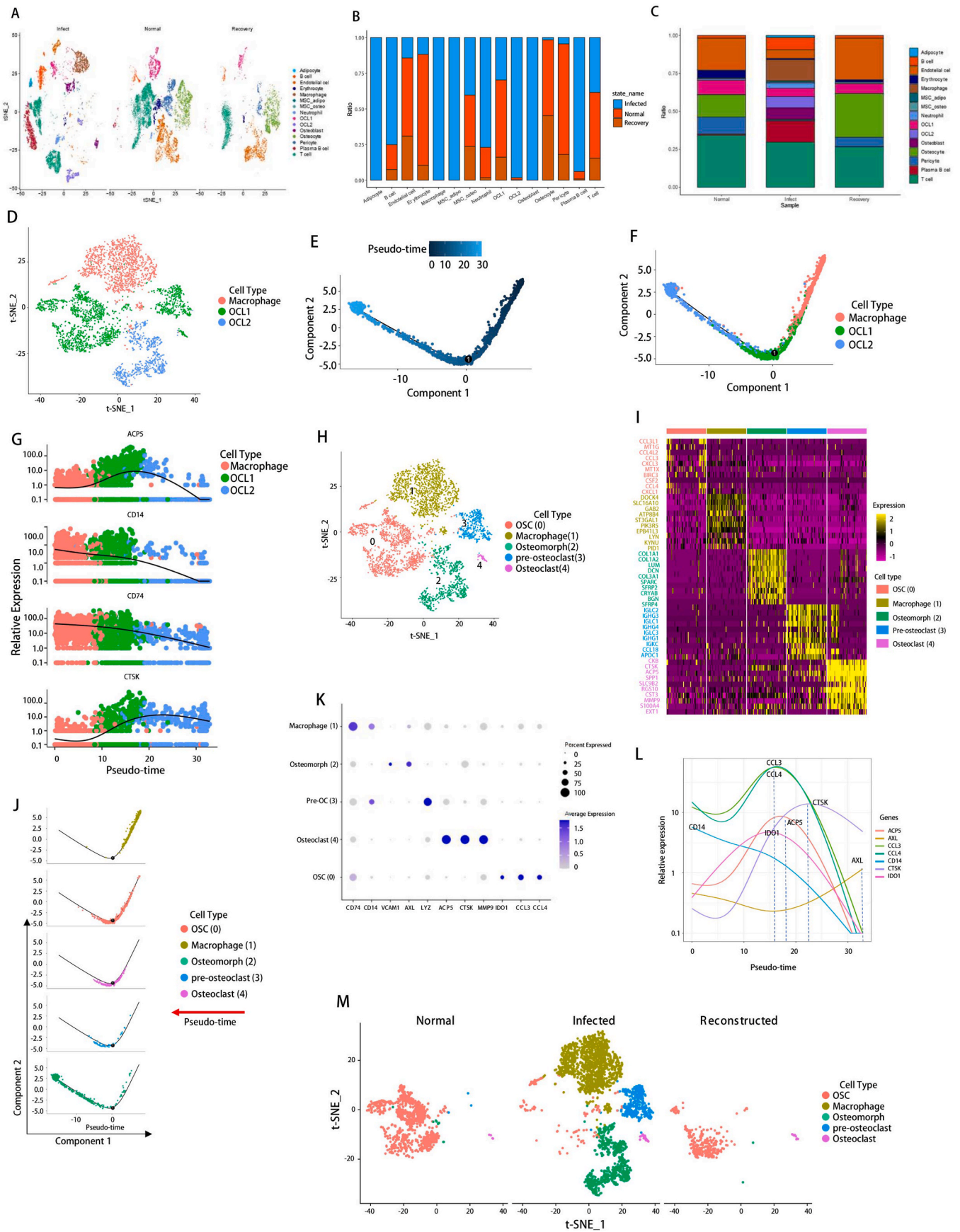
2.1. Cellular heterogeneity among normal, infected, and reconstructed cortical bone tissues with scRNA-seq

We performed scRNA-seq on 5 bone samples, including 2 normal cortical samples, 2 infected bone samples and 1 reconstructed bone sample (SM. Table 1), to investigate the cellular heterogeneity between the physical and pathological bone environments (Fig. 1A). Cases were diagnosed as OM by X-ray, CT, MRI, and radionuclide bone imaging (Fig. 1B). After quality control and data filtering, we obtained 30,947 deeply sequenced cells, consisting of 12,921 cells from the normal cortical limb samples, 12,435 cells from the osteomyelitis lesions, and 5591 from the reconstructed sample. After tabulation of the cell-by-gene expression matrix, we performed dimensionality reduction by t-stochastic neighbourhood embedding (t-SNE) and graph-based clustering (see method "Cell type annotation"). Overall, 20 cell clusters were

identified when all 30,947 cells were considered as a whole (Fig. 1C) [16]. The defining individual clusters were defined by comparison to known lineage or canonical markers (Fig. 1D). As a result, the 20 clusters could be divided into 15 cell types, including 13 canonical and 2 non-canonical cell types (Fig. 1D and SM. Fig. 2). The bone tissue consisted of 13 canonical cell types: (1) osteocytes with high expression of LUM and COL1A2; (2) T cells specifically expressing CD3D and CD3E; (3) endothelial cells characterized by high SELE, FABP4 and vWF expression; (4) B cells with high expression of CD79A and CD79B; (5) pericytes with high expression of ACTA2, RGS5 and MCAM; (6) erythrocytes with characteristic high HBB and HBA1 expression; (7) neutrophils specifically expressing BCL2A1, S100A8 and CXCL8; (8) plasma blasts with high expression of JCHAIN; (9) osteoblasts with high expression of COL3A1 and COL1A1; (10) macrophages specifically expressing CD14 and HLA-DRA; (11) adipocytes with high expression of PPAR γ and AHR; (12) MSC-osteo with high expression of THY1, COL1A2, and ENG; and (13) MSC-adipo characterized by relatively high expression of PPAR γ , THY1, and ENG (Fig. 1D and SM. Fig. 3). To reveal the specific characteristics of these clusters, we performed gene ontology (GO) and Kyoto Encyclopedia of Genes and Genomes (KEGG) pathway enrichment analyses using the top 100 DEGs of each identified cell cluster, consistent with the well-known functions of those canonical cell types (SM. Fig. 4). In addition to the 13 classic cell types, we next focused on the two noncanonical types of cells. Cluster 4 was termed CD14^{hi} ACP5^{hi} CTSK^{mid} osteoclast-like cell 1 (OCL1), as it expressed high levels of CD14, which was not expressed in classic osteoclasts (Fig. 1D). The biological functions of OCL1 were enriched in Cell chemotaxis, Myeloid leukocyte migration and cytokine–cytokine receptor interaction (SM. Fig. 4). Cluster 12 was characterized as CD14^{neg} ACP5^{mid} CTSK^{hi} osteoclast-like cell 2 (OCL2), as ACP5 expression in this cluster was not the highest among the clusters (Fig. 1D). The biological functions of OCL2 were enriched in extracellular matrix organization, cartilage development and collagen fibril organization (SM. Fig. 4).

2.2. Identification of $Ido1^{high}CCL3^{high}CCL4^{high}$ osteostaticytes at the earlier stage during osteoclast differentiation

We next set out to determine the compositional differences of cell types among the three sample groups (Fig. 2A, B and 2C). Both the normal and reconstructed cortical bone tissue consisted of only 11 out of the 15 cell types identified. Macrophages and adipocytes were not identified, suggesting a low level of inflammation in normal cortical bone tissue (Fig. 2A and C). Specifically, endothelial cells accounted for 21 and 27 % of the total cell population in normal and reconstructed bone tissue, respectively. In addition, pericytes also contributed 11 % and 6 % of the cell population in normal and reconstructed bones, respectively (Fig. 2C), highlighting that blood supply is of great importance in these bone tissues [17]. More interestingly, in both normal and reconstructed bone samples, immune cells remained a large component, constituting over 30 % of the total cells. Among the immune cells, T cells were the most abundant (Fig. 2C). The infected bone tissues consisted of all 15 cell types (Fig. 2A and C). Compared with the normal and reconstructed bone samples, macrophages, adipocytes, and osteoblasts existed only in OM tissue (Fig. 2C). In addition, the percentages of B cells, plasma blasts and OCL2 increased significantly in OM samples, and the percentages of endothelial cells and OCL1 decreased



(caption on next page)

Figure 2. Identification of IDO1^{high}CCL3^{high}CCL4^{high} osteostaticytes during osteoclast lineage differentiation A) t-SNE plot showing the three main cell types of osteoclast lineage cells. B) Monocle 2 trajectory plot showing the pseudotime curve of the whole osteoclast lineage. C) Monocle pseudospace trajectory revealing the dynamics and distribution of macrophage, OCL1 and OCL2 subclusters. D) Pseudotemporal expression dynamics of specific marker genes (ACP5, CD14, CD74 and CTSK). All single cells in the macrophage, OCL1 and OCL2 cell lineages are ordered based on pseudotime. E) t-SNE plot showing 5 reclustered subclusters of the osteoclast lineage in cortical bone lesions (osteostaticytes 0, macrophages 1, osteomorphs 2, preosteoclasts 3 and osteoclasts 4). F) Heatmap depicting the average expression levels per cluster of the top differentially expressed markers in 5 subclusters. G) Monocle 2 trajectory revealing the distinct pseudospace distribution and order of 5 subclusters. H) Dot plots showing the expression of the 11 signature genes across the 5 subclusters. The size of the dots represents the proportion of cells expressing the particular marker, and the colour spectrum indicates the mean expression levels of the markers. I) Monocle 2 trajectory revealing distinct marker gene expression patterns along with pseudotime (ACP5, AXL, CCL3, CCL4, IDO1, CD14 and CTSK). J) The t-SNE plot divided by 3 distinct sample states (normal bone, infected bone and reconstructed bone) depicting 5 subclusters in human cortical bone lesions.

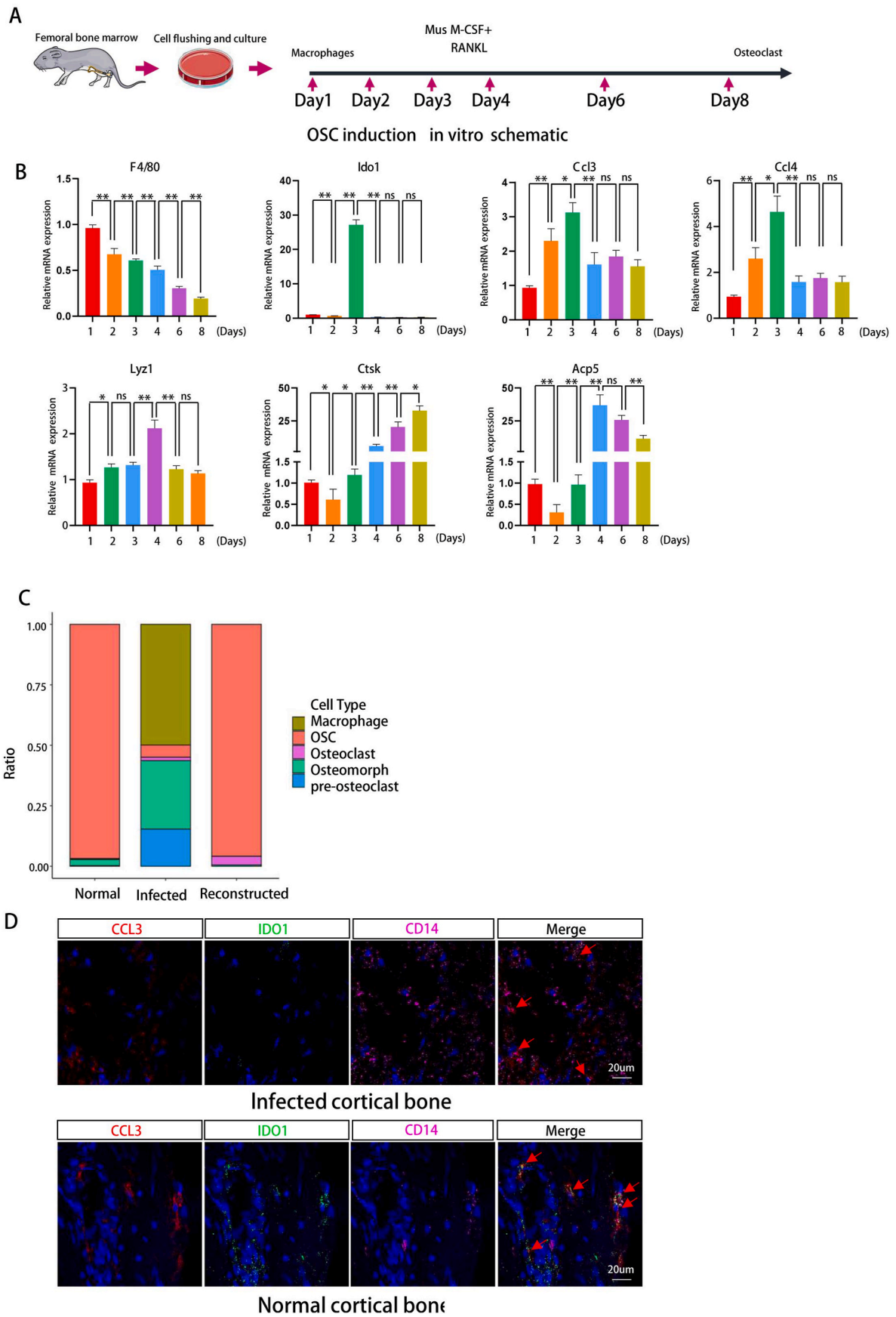
significantly. However, osteocytes, pericytes and erythrocytes were not identified in the OM tissue. The cell component changes in infected bone tissues suggested pathological changes, including bone destruction, impaired blood supply and avascular tissue [18]. However, the inflammation and remodelling of bone were obviously increased due to increased macrophage, osteoblast and OCL2 infiltration [19,20]. Moreover, there was a subtle increase in the number and proportion of MSC_osteoclast cells in reconstructed bone samples (Fig. 2B).

We then shifted our attention to osteoclast lineage cells (Fig. 2D). To determine whether these three clusters of cells (OCL1, OCL2, and macrophages) belong to the same cell lineage, we constructed a pseudotime developmental tree via the inferred differentiation trajectories among 3 distinct clusters (Fig. 2E). The results revealed a trajectory starting with macrophages, bifurcating into the OCL1 subset, and ending in the OCL2 subset, suggesting that these cells belong to the same lineage (Fig. 2F). According to the Monocle 2 algorithm, myeloid markers such as CD14 and mature osteoclastic markers, including ACP5 and CTSK, exhibited distinct expression patterns along the trajectory axis (Fig. 2G). The results showed that the expression of CD14 and CD74 continuously decreased along the pseudodifferentiation axis, and macrophages were mainly applied early in the lineage (Fig. 2G). The expression of ACP5, the most critical marker of osteoclasts, started at a low level, reaching a peak followed by a gradual decrease to an undetectable level upon full OC differentiation. Interestingly, the level of CTSK was similar to that of ACP5, with only a small reduction at the end (Fig. 2G). The trend of the changes in the transcription of these key genes is very consistent with the process of osteoclast differentiation. To increase the resolution in defining the cell components among macrophages, OCL1 and OCL2, we obtained all osteoclast lineage cells and performed dimensionality reduction by t-distributed stochastic neighbour embedding (t-SNE) and graph-based clustering again. The original three subsets formed five distinct clusters (Fig. 2H). We then compared the results with the previous dimensionality reduction map and found that there was no significant difference in the number or distribution of macrophages or OCL2 after the refined dimensionality reduction (Fig. 2H). However, the previously identified OCL1 was further divided into three subclusters, namely, clusters 0, 3, and 4 (Fig. 2H). We annotated the five clusters by comparing the top 10 DEGs defining each lineage marker to known lineage markers (Fig. 2I). According to the results of the pseudotime developmental tree analysis, the trajectory differentiation order of these 5 clusters was macrophages (1), cluster 0 (0), cluster 3 (3), cluster 4 (4), and cluster 2 (2) (Fig. 2J). Here, we compared the expression trends of several specific markers of the osteoclast lineage along with clusters and pseudotime, including those of CD14, CCL3, CCL4, IDO1, ACP5, CTSK and AXL (Fig. 2K and L). As expected, the expression of CD14, a monocyte/macrophage-specific marker, continuously decreased during differentiation and eventually became undetectable. In contrast, the level of AXL, a marker of osteomorphs, continued to increase over time (Fig. 2L) [21]. CCL3 is a macrophage inflammatory protein known to stimulate osteoclastogenesis [22,23]. CCL3 expression started at a moderate level, reaching a peak, followed by a sharp decrease to undetectable levels upon full OC differentiation (Fig. 2L). Compared with the other 4 clusters, we identified IDO1 as a specific marker gene in cluster 0. The expression pattern of IDO1 was similar to that of CCL3 and CCL4, and its peak point was slightly ahead of the ACP5 peak

(Fig. 2L). Strikingly, the expression pattern of ACP5 was concordant with that of CCL3, suggesting that ACP5 is important for early osteoclast lineage differentiation (Fig. 2L). Last, the expression trajectory of CTSK was similar to that of CCL3 and ACP5 despite an apparent phase lag (Fig. 2L). Therefore, we could still observe a rather high level of CTSK expression at the end of pseudotime (Fig. 2L). We speculated that CTSK is important for the late stage of macrophage-OC lineage differentiation and OC maintenance. Based on the expression level of the key marker genes, cluster 3 cells fit the functional requirement of preosteoclasts (pre-OCs) with the characteristic ACP5^{hi}, CD14^{mid} CTSK^{mid} expression. Supporting this notion, cluster 3 cells originated from macrophages (cluster 1) in the pseudotime course (Fig. 2K) [20,24]. In addition, we speculated that cluster 4 cells serve as bona fide osteoclasts because cluster 4 cells exhibited the highest expression of osteoclast markers (CTSK, MMP9 and ACP5) (Fig. 2K). Osteoclasts are multinucleated cells that need to be maintained at only a small amount in bone tissue to play a role in bone resorption [25]. Indeed, there were only 65 osteoclasts in all the samples, and most of them were found in the infected bone tissues (Fig. 2M). Osteomorphs are a distinct cell type that are produced by fission from osteoclasts to prevent apoptosis and keep osteoclasts alive [21]. Multiple osteomorphs can quickly fuse to form OCs if necessary [21]. Pseudotime analysis showed that OCL2 was derived from OC (or cluster 4), therefore fitting the description of osteomorph cells (Fig. 2J). We then examined the expression of two osteomorph markers (AXL and CADM1) in cluster 2 cells and found that their expression was the highest among the other subclusters (Fig. 2K) [21].

While 4 out of 5 cell clusters could be assigned to a known cell type along the macrophage-OC axis, cluster_0 represented a novel cell subset at the earlier stage. In particular, cells in cluster 0 expressed high levels of macrophage inflammatory proteins (CCL3 and CCL4) and moderate levels of a matrix degradation protein (MMP9) but low levels of monocyte (CD14) and OC (CTSK or ACP5) markers and hence could not be defined as any specific classic cell type (Fig. 2K and L). RANK is the specific receptor for RANKL. We also compared the relative mRNA expression of TNFRSF11A (RANK) among osteoclast lineages. In the osteoclast lineage, all the subsets showed varying levels of TNFRSF11A expression. However, osteoclasts exhibited the highest expression of the TNFRSF11A gene. OSCs had lower expression levels than osteoclasts but still had higher expression levels than other subsets (SM. Fig. 5). This indicates that OSC cells also express the RANKL receptor at a significant level and respond to RANKL. Given that cluster_0 cells were positioned between macrophages and pre-OC in the pseudotime analysis, they may represent a pool of cells critical for bone homeostasis. More strikingly, most of the cluster_0 cells existed in the normal and reconstructed cortical bone tissues, and they were more abundant than OCs in those samples (Fig. 2J). While cluster_0 cells are clearly needed for normal bone homeostasis, it is plausible that the reservoir of cluster_0 cells is partially/fully depleted as cluster_0 cells shift towards OC differentiation under infection conditions. We therefore named the cluster_0 cells “osteostaticytes” or OSCs for short. Moreover, compared with other cell types among cortical bone tissues, the mRNA expression of IDO1, CCL3 and CCL4 was highest in OSCs; thus, we named these cells IDO1^{high}CCL3^{high}CCL4^{high} OSCs (Fig. 2J).

According to the pseudotime results, OSC cells exist at an earlier stage of osteoclast differentiation. Therefore, we constructed an



(caption on next page)

Figure 3. Validation of the existence of OSCs in vitro and in vivo. **A)** OSC induction schematic in vitro with 25 ng/ml M-CSF and 100 ng/ml RANKL. **B)** Relative mRNA expression of monocyte/macrophage lineage marker genes (ACP5, CCL3, CCL4, IDO1, CD14 and CTSK) at 6 different time points during OSC induction via RT-qPCR analysis of mouse bone marrow monocytes. All the data are shown as the means ± SDs. ** $P \leq 0.01$, * $P < 0.05$; NS, not significant ($P > 0.05$) **C)** Histogram depicting the relative proportion of each osteoclast lineage subset among the respective sample states in all cortical bone lesions as indicated. **D)** Immunofluorescence staining of OSC markers in normal cortical bone tissues. Serial sections were stained for CCL3 (red) and IDO1 (green); serial sections were stained for CD14 (red), CCL4 (pink) and IDO1 (green); and infected cortical bone sections were stained for CD14 (red). Scale bars: 20 μm (upper and bottom). The area indicated by the red arrow is the colocalated area.

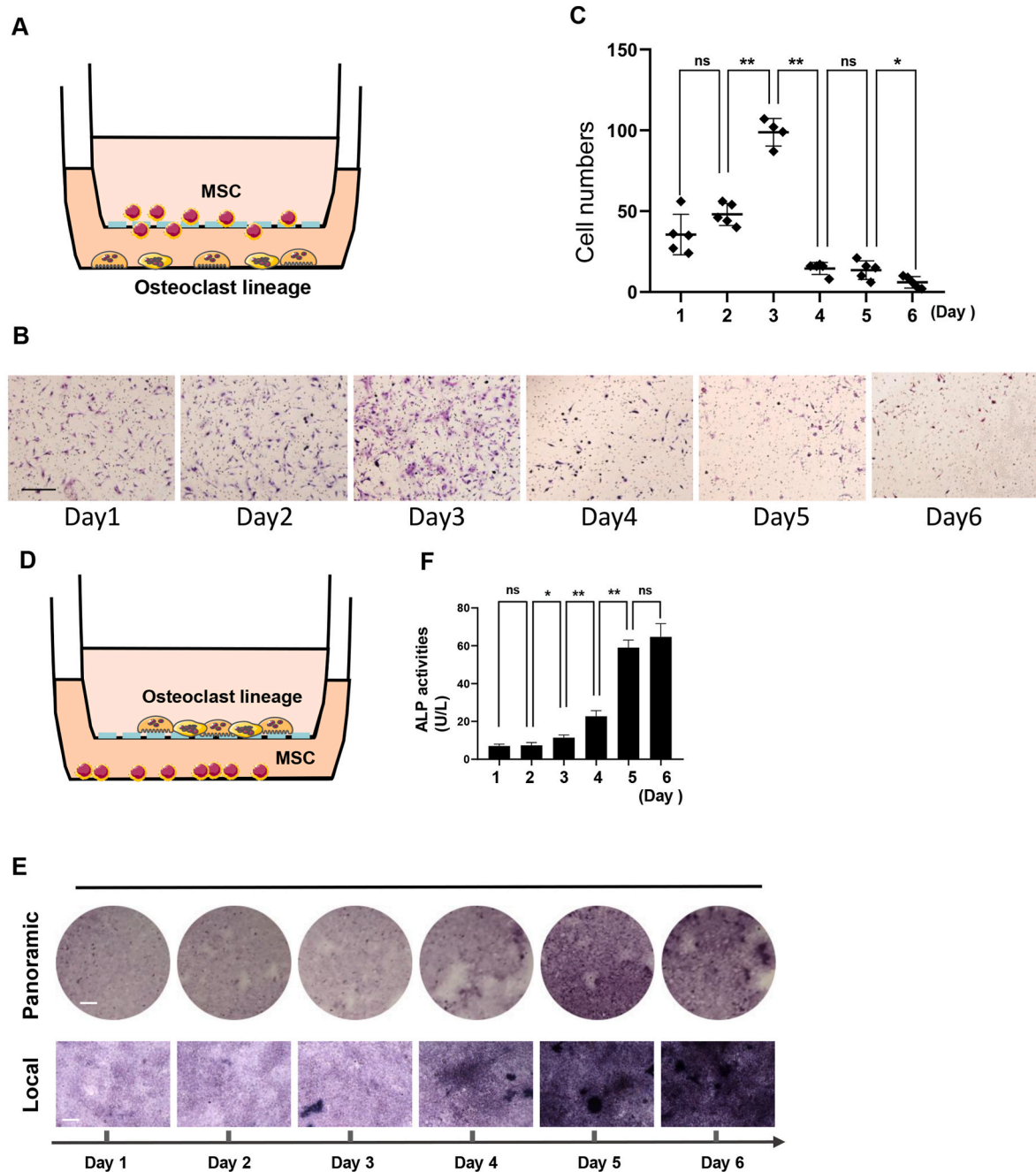


Figure 4. Cells at the earlier stage of osteoclast lineage contribute to MSC recruitment **A)** Schematic diagram of the Transwell assay. MSCs were seeded in the upper well, and osteoclast lineage cells were seeded in the lower well; **B)** Transwell migration assay of each osteoclast lineage at different time points; **C)** Analysis of the number of migrated MSCs when cocultured with different osteoclast lineage cells (from day 1 to day 6); Scale bars: 200 μm ; **D)** Schematic diagram of the coculture assay. MSCs were seeded in the upper well, and osteoclast lineage cells were seeded in the lower well; **E)** Representative images of ALP staining (panoramic and local) of MSCs under osteogenic and adipogenic induction. Scale bars: 200 μm (upper), 50 μm (bottom). **F)** Quantification of integrated optical density (IOD) for ALP staining for the six groups ($n = 3$). All data are shown as the mean ± SD. ** $P \leq 0.01$, * $P < 0.05$; NS, not significant ($P > 0.05$).

Figure 5. Functional investigation via GSEA and CellChat analysis of osteoclast lineage. **A)** GSEA of distinct pathways of 5 subsets among osteoclast lineages, including bone resorption, bone mineralization, mesenchymal cell differentiation, bone development, chemotaxis activity, and mesenchymal cell chemotaxis. The red line refers to OSC, the purple line refers to osteoclast, the blue line refers to pre-OC, the green line refers to osteomorph, and the brown line refers to macrophage. **B)** NES scores of individual pathways among 5 subsets. (# represents that the p value of this pathway is over 0.05). **C)** Violin plot of the gene expression distribution of chemotaxis signature-related genes, including CCL3, CCL4, CCL20, CCL22, CCL3L1, CXCL8, and CXCL12, among 5 distinct subsets. **D)** Violin plot of the gene expression distribution of osteogenesis signature-related genes, including COL1A1, BMP2, BGN, MMP13, and SIGLEC15, among 5 distinct subsets. **E and F)** Comparison of the outgoing and incoming interaction strengths in 2D space to identify the cell populations with significant changes in sending or receiving signals in the CCL pathway (E) and PERIOSTN pathway (F). The size of the dots represents the counts of signal density.

osteoclast induction model using bone marrow monocytes and detected dynamic changes in the expression of genes related to osteoclast lineage differentiation, including F4/80, Ido1, Ccl3, Ccl4, Ctsk, Lyz1 and Acp5, in vitro (Fig. 3A). The results showed that CD14 expression constantly decreased during differentiation. OSC highly expressed genes, including IDO1, CCL3 and CCL4, were significantly upregulated at the earlier stages and then downregulated (Fig. 3B). The specific OC marker genes ACP5 and CTSK were highly expressed at the later stage (Fig. 3B). These results were nearly in accordance with the scRNA-seq results in the pseudotime trajectory, suggesting that OSCs indeed existed at the stage of osteoclast differentiation. In addition, we analysed the distribution of osteoclast lineage cells among the three different states. OSCs account for the vast majority of normal and reconstructed bones (Fig. 3C). The macrophages, pre-OCs and osteomorphs were mainly present in infected bone (Fig. 3C). To further confirm the presence of OSCs in cortical bone, we used immunofluorescence (IF) staining to detect the protein expression of several genes highly expressed in OSCs, including IDO1 and CCL3 (Fig. 3D). The IF staining results in normal cortical bone revealed that CCL3 and IDO1 were coexpressed mainly in the same regions (Fig. 3D). However, almost no expression of IDO1 in infected cortical bone was detected, suggesting that there were few OSCs under these conditions, consistent with the scRNA-seq results (Fig. 3D). To preliminarily investigate the relationship between infection and the presence of OSCs, we opted to use Staphylococcal Protein A (SPA) as a virulence factor substitute for *S. aureus* in our cocultures. We conducted cocultures for 2, 4, and 6 days. The results indicated that SPA treatment significantly downregulated IDO1 gene expression after both 2 and 4 days of osteoclast induction, suggesting that infection may inhibit the development or formation of OSC cells (SM. Fig. 6). In addition, we reanalyzed the sequencing dataset deposited from the human femoral head [26]. Notably, the highest expression of IDO1 was detected in Cluster 6 (SM. Fig. 7A and 7B). Pseudotime analysis suggested that the temporal trends of key marker genes across all osteoclast lineage cells perfectly aligned with our data (SM. Fig. 7C). These results further validated the existence of OSC cells within the osteoclast lineage.

2.3. Cells at the earlier stage of osteoclast lineage contribute to MSCs recruitment

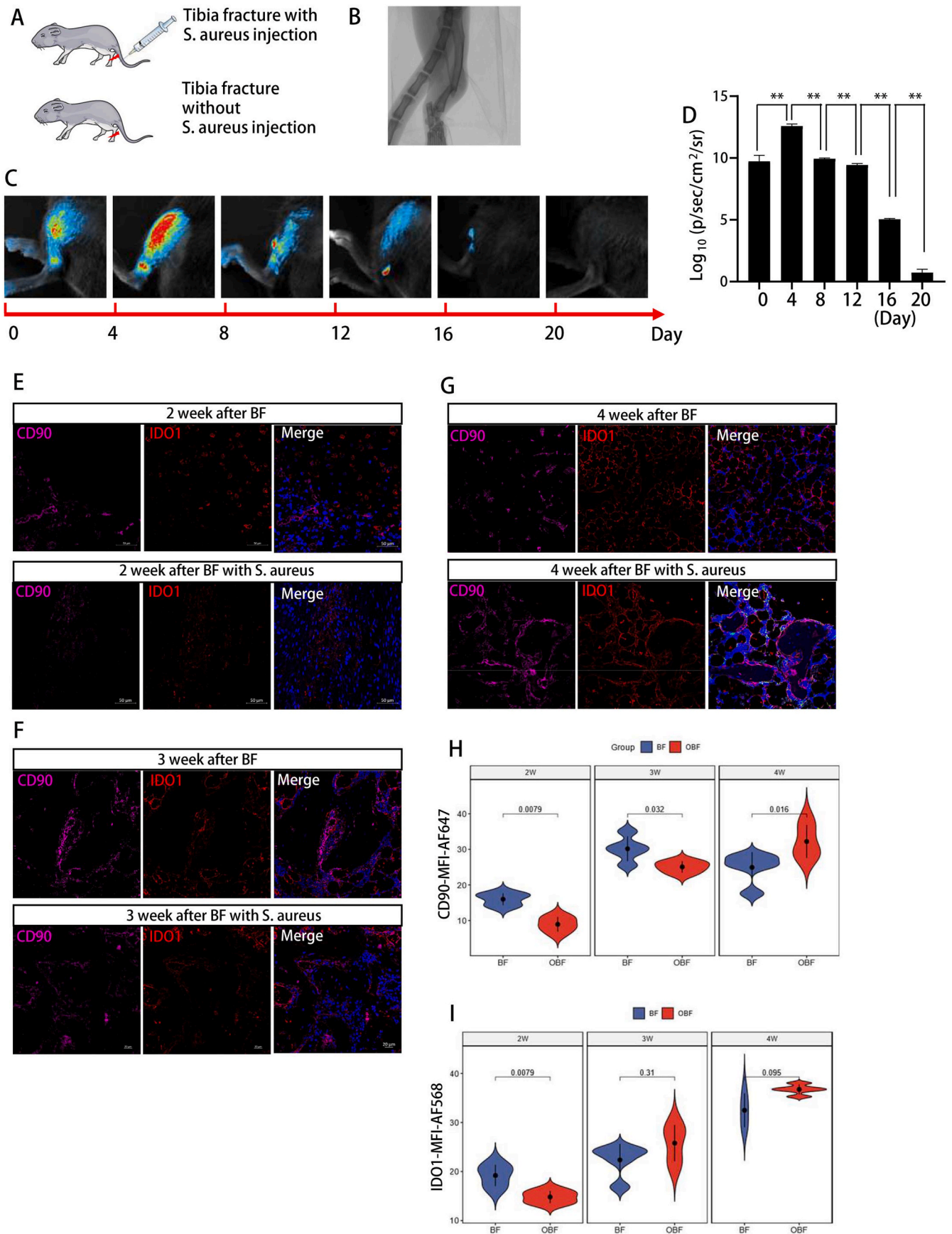
To assess the dynamic function of the osteoclast lineage, we first isolated bone marrow monocytes and then induced them with M-CSF and RANKL for 6 days to obtain cells at different differentiation stages from monocytes to osteoclasts. We then performed a transwell assay to test the migration of MSCs cocultured with these cells at each time point (Fig. 4A). Quantitative analysis revealed that the migration of MSCs induced by the cells on day 3 (98 ± 7.55 cells/day) was significantly greater than that induced by the other time points (Fig. 4B and C) and then decreased after day 4 (Fig. 4C). We also investigated the impact of osteoclast lineage on the osteogenic differentiation of MSCs at different time points via another coculture system (Fig. 4D). The ALP activity results suggested that during the differentiation of osteoclast lineage cells, the effect of these cells on osteogenic induction gradually increased (Fig. 4E and F). CCL3 and CCL4 are highly expressed in OSCs, and these chemokines may serve as crucial factors in the chemotactic function of OSCs. To investigate this possibility, we used maraviroc, a specific CCR5 antagonist that inhibits the chemokine receptors CCL3, CCL4, and CCL5, on early-stage mononuclear cells induced in vitro. As

CCL5 was nearly expressed in OSCs, maraviroc mainly blocked the effects of CCL3 and CCL4 in this assay. Following treatment, OSCs, along with MSCs, were subjected to a transwell migration assay (SM. Fig. 8). The results demonstrated that the addition of Maraviroc significantly reduced the chemotactic ability of mononuclear cells towards MSCs. This finding suggested that CCL3 and CCL4 are key chemotactic factors in OSCs (SM. Fig. 8). Taken together, our results suggest that these cells in the early stage of osteoclast lineage differentiation might be critical for the reversal phase through recruiting MSCs.

2.4. OSCs may serve as reversal cells in bone remodelling

To further estimate the chemotaxis ability or osteogenic potential of osteoclast lineage subsets, we performed gene set enrichment analysis (GSEA) on the DEGs among these five subsets. The GSEA results showed that the DEGs in macrophages obtained the highest normalized enrichment scores (NES) in gene sets, including the regulation of phagocytosis and regulation of leukocyte apoptosis, compared to the other four subsets (Fig. 5A and B). Additionally, we compared the NESs of the bone resorption gene sets, and the results showed that the DEGs in osteoclasts had the highest score, followed by those in pre-OCs (Fig. 5A and B). To determine the relationship between OSCs and osteoclast-related pathways, we analysed the enriched pathways and signals and found that there were no pathways related to NF- κ B or osteoclast differentiation in OSC cells. Moreover, we performed a bone resorption assay to evaluate the potential role of the OSC, which indicated that calcium phosphate absorption was minimal after 3 days of induction. However, significant bone resorption was observed on day 6. These findings suggest that OSC cells may not possess strong bone resorption capabilities (SM. Fig. 9). The DEGs in the OSC had the only positive and highest scores in gene sets, including mesenchymal cell chemotaxis and chemokine activity (Fig. 5A and B). These two gene sets showed a trend of first increasing and then decreasing if all five subsets were ordered in trajectory pseudotime (Fig. 5A and B), consistent with the results of transwell experiments in vitro (Fig. 4B). A violin plot showed that the genes enriched in chemotaxis signatures, including CCL3, CCL4, CCL20, CCL22, CCL3L1, CXCL8 and CXCL12, were highly expressed in OSCs (Fig. 5C). We also analysed several osteogenesis-related gene sets, including genes related to osteoblast differentiation, bone development, mesenchymal cell differentiation, and bone mineralization, and found that the NES tended to gradually increase among these five subsets, consistent with the in vitro results of cell–cell coculture assays (Fig. 5A, B and Fig. 4B). As expected, genes enriched in osteoblast differentiation and bone development signatures, such as BMP2, SIGLEC15, COL1A1, and POSTN, were highly expressed in osteomorphs and osteoclasts (Fig. 5D). We further investigated the cellular interactions among osteoclast lineage subsets and osteoblast lineage subsets in bone environments using CellChat, a cell ligand/receptor pairing-based database. The results showed that OSCs were the dominant communication source in the outgoing signals of CCL, which suggested that OSCs might be the most significant chemotactic cells (Fig. 5E). We then focused specifically on the periostin signals related to osteogenesis and observed a pronounced increase in the number of outgoing signals in the osteomorphs (Fig. 5F). The CellChat and GSEA results indeed suggested that OSCs might play an important role in MSC chemotaxis, which might function in bone reversal.

Due to the potential critical role of OSCs in bone reversal and the significant decrease in the number of infected cortical bone, we propose



(caption on next page)

Figure 6. OSCs are sufficient for the occurrence of bone mesenchymal stem cells during bone remodeling. **A)** Schematic diagram of the tibia fracture model. **B)** Representative radiographs of the mouse fracture model via X-ray. **C)** USA300/Eno-Antares2 tracing bacteria showed the infection condition of fracture lesions every 4 days. **D)** Bar plot of infection conditions among each time point with USA300/Eno-Antares2 tracing bacteria. All data are shown as the mean \pm SD, $n = 5$. $**P \leq 0.01$, $*P < 0.05$; NS, not significant ($P > 0.05$). **E, F and G)** Immunofluorescence staining of IDO1 (red) and CD90 (purple) in normal fracture lesions and infected fracture lesions were stained in sections; E for 2 weeks after fracture, F for 3 weeks after fracture, G for 4 weeks after fracture; Scale bars: 50 μm . **H and I)** The violin graph shows the statistical results of purple fluorescence intensity (CD90-AF647 nm) representing the number of MSCs (H) and red fluorescence intensity (IDO1-AF568 nm) representing the number of OSCs (I). ($n = 5$) P values are displayed over the data. BF represents the normal fracture group, and OBF represents the infected fracture group.

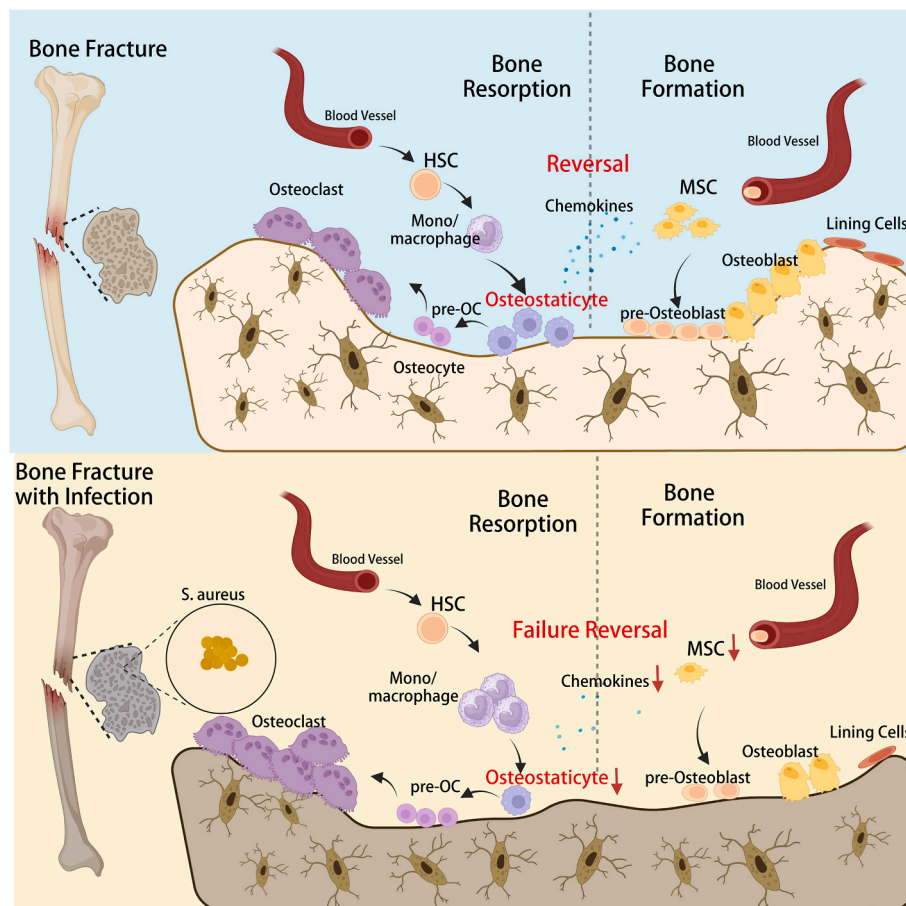


Figure 7. Schematic diagram showing the role of osteostaticytes (OSC). Monocyte-derived macrophages, primarily in the form of OSCs, stably reside in cortical bone. When bone remodelling is initiated, OSCs can recruit many osteoprogenitor cells to the site of reconstruction via chemotaxis. OSCs themselves can further differentiate into osteoclasts, facilitating bone resorption while simultaneously undergoing osteocytic coupling. As bone resorption is completed, the recruited osteoprogenitor cells can be induced by osteoclasts or osteomorph cells to differentiate into mature osteoblasts, thereby achieving a coordinated process of bone resorption and formation (**upper diagram**). If the survival stage of OSCs in the bone remodelling microenvironment is shortened or restricted, osteoprogenitor cells cannot be effectively recruited to the site of reconstruction, leading to delayed or impaired bone repair due to failure reversal (**bottom diagram**).

that fewer OSCs triggered by infection might be responsible for the impaired bone remodelling. Thus, we constructed tibia fracture models with/without infection to determine the relationship between the OSC and bone remodelling. First, a closed lower-shaft tibia fracture mouse model was generated via three-point bending (Fig. 6A). Next, 2 μl of *S. aureus* solution at 1×10^5 CFU/ml was injected into the fracture site of the infected group. The fracture status was detected by microcomputed tomography (micro-CT) (Fig. 6B). We employed a fusion luciferase-labelled *S. aureus* tracing system to detect infection in real time in vivo (Fig. 6C and D). The fluorescence intensity results revealed that the *S. aureus* infection dramatically increased in the first week, gradually decreased in the second week, and finally disappeared in the third week after injection (Fig. 6D). MicroCT analysis revealed that the bone callus at the fracture site of the infected group of mice was not fully mineralized, suggesting that impaired bone remodelling occurred in the infected group (SM. Fig. 10). Then, we aimed to determine the relationship

among MSCs marked with CD90 and OSCs marked with IDO1 during bone remodelling progression via multiplex fluorescence staining. The results revealed that the expression level of CD90 was obviously greater in the 2-week normal fracture group but significantly decreased in the 2-week infected bone fracture group (Fig. 6E and H). Moreover, the expression level of IDO1 was similar to that of CD90 (Fig. 6E and I). After 3 weeks, the infection was nearly eliminated, and the levels of CD90 and IDO1 started to increase in the infected bone fracture group (Fig. 6F, H and 6I). The fluorescence staining results revealed that the levels of CD90 and IDO1 continuously increased in the 4-week infection group (Fig. 6H and I). These data indicated that OSCs and MSCs returned and functioned regularly in bone remodelling progression after infection elimination. By week 4, the number of osteoclasts in the control fracture group was significantly lower than that in the infected fracture group, indicating that the normal fracture group had already progressed to mineralization. Consequently, the bone trabeculae begin to reshape, and

excess callus is absorbed by osteoclasts (SM. Fig. 11). The infection group seemed to have experienced delayed union compared to the normal group (SM. Fig. 11). The dynamic results indicated that the presence of OSCs seems to be related to the presence of MSCs and may play a critical role in bone reversal coupled with the presence of MSCs.

3. Discussion

In bone remodelling, the well-orchestrated coupling phase maintains bone homeostasis, including balanced bone resorption and formation, appropriate regulation of calcium and phosphorus metabolism, and regulation of individual bone cell activity [27]. However, the mechanism of bone reversal remains elusive. In particular, the nature of the original dispute of reversal cells. In this study, we found that early-stage osteoclast lineage cells recruit MSCs and that their osteogenic induction ability increases with the differentiation of the osteoclast lineage in vitro. Using scRNA-seq, we identified an earlier stage called IDO1^{high}CCL3^{high}CCL4^{high} OSCs within the osteoclast lineage by analysing the differentiation trajectory pseudotime. Then, we confirmed the presence of OSCs via immunofluorescence staining of cortical bone tissue and real-time PCR of differentiated osteoclast lineage cells. To our surprise, bioinformatic analysis revealed that OSCs exhibited the highest chemotactic activity, which was confirmed by GSEA and CellChat analysis. In a mouse model, OSCs were found to be positively related to bone MSC occurrence and bone remodelling. Combining these findings, we propose that OSCs are a novel subset at an earlier stage during the osteoclast lineage and might be reversal cells. Consequently, the name “osteostaticytes” derives from combining “osteo” (related to bone) and “-static” (suggesting stability or maintaining balance), reflecting their proposed function in maintaining bone homeostasis and structure.

The origin of reversal cells is still a controversial topic. Our findings are in accordance with some studies indicating that the “reversal” cells are from osteoclast lineage cells. Initially, “reversal” cells were suggested to be monocytic phagocytes based on morphological assessment [9]. Studies have shown that macrophages contribute to the recruitment of MSCs and osteoprogenitors to fracture sites by secreting CCL2, CXCL8 and SDF-1 [28]. Studies have also reported that macrophages engage in both intramembranous bone formation and endochondral bone formation by regulating osteoblast mineralization and gene expression [29, 30]. Chang and colleagues reported that resident bone macrophages were located immediately adjacent to mature osteoblasts at sites of active bone modelling [31]. Impressively, more than 75 % of osteoblasts on the endosteal surface of cortical bone are covered by a canopy-like structure of F4/80⁺, CD68⁺, Mac-3⁺, or TRAP⁺ macrophages [32]. A similar population was described in human bone, suggesting a significant role in supporting bone formation [31]. In addition, both pre-osteoclasts and osteoclasts play critical roles in promoting osteogenesis by secreting extracellular vesicles [33]. These data provide clear evidence that the monocytic osteoclast lineage plays significant roles in the recruitment and differentiation of osteoblastic cells, which is potentially helpful in bridging the transition between bone resorption and formation. Nevertheless, the opposite view insists that the reversal cell is from the osteoblast lineage based on its morphology and local positive markers, ALP positive and MOMA2 negative [10,34]. However, studies have reported that MOMA2-positive cells and F4/80-positive cells are distinct monocytic cells [35]. Recently, macrophages have been shown to exhibit alkaline phosphatase expression [11]. Our results revealed that some osteoclast lineage cells had positive ALP expression (SM Fig. 12). Previous studies have found that the NF- κ B pathways were critical in osteoclast formation [36]. Here, our results revealed that differentiated expressed genes in OSCs were also enriched in canonical NF- κ B pathway and the key genes such as TRAF6 and SQSTM1 were also relatively higher in OSC cells (SM Fig. 13). These data suggested that OSCs indeed had similar signalling activities such as NF- κ B pathway with osteoclast. The communication mechanism by which bone formation follows bone resorption is referred to as coupling, which is

analogous to how a train carriage follows an engine. From the perspective of functional needs, some authors suggest that reverse cells are phagocytic macrophage-like cells, as they can phagocytose demineralized collagen or other matrix molecules left by osteoclasts in the resorption lacuna [37–39]. Osteoclasts serve as the driving force behind remodelling, acting as the engine, while osteoblasts, through coupling, act as the cellular carriage that follows. Therefore, according to the sequence of events related to bone remodelling, bone coupling should logically be undertaken by osteoclast lineage cells.

After determining the nature of the reversal cells, the exact nature of the coupling signal that coordinates this transition and directs bone formation specifically to sites of bone resorption is still a subject of debate and controversy. The initial proposed mechanism for coupling signals was the release of growth factors stored in significant quantities within the bone matrix during the process of resorption. Insulin-like growth factors I and II, as well as TGF- β , are examples of factors that are involved in the coupling mechanism. The active regulation of TGF- β seems to play a crucial role in signalling the recruitment of mesenchymal stem cells to sites of bone resorption [40]. However, this hypothesis was neglected because in mice and humans with dysfunctional osteoclasts that cannot resorb bone, osteoblast bone formation remains intact despite the absence of matrix-bound growth factors [41]. Thus, the hypothesis that osteoclasts produce coupling factors has emerged. Two main coupling mechanisms have been proposed, including the soluble molecule sphingosine 1-phosphate (SGPP1) and the cell-anchored EphB4-ephrin-B2 bidirectional signalling complex. SGPP1 is secreted by osteoclasts, induces osteoblast precursor recruitment, and promotes the survival of mature osteoblasts [42]. Hence, our results showed that SGPP1 was more highly expressed in macrophages other than osteoclasts than in those of osteoclast lineages (SM. Fig. 12). This finding suggested that osteoclasts do not play critical roles in osteoblast precursor recruitment. EphB4 receptors are expressed on osteoblasts, whereas osteoclasts express the ligand ephrin-B2 (EFNB2). Forwards signalling through EphB4 to osteoblasts enhances osteogenic differentiation [43]. Our data indicated that EFNB2 was significantly highly expressed in osteomorphs (SM. Fig. 12). These results suggest that cells located in the late stage of osteoclast differentiation produce more EFNB2, thereby promoting osteogenesis. Overall, determining the real origin of reversal cells is the key to investigating the detailed coupling mechanism.

OM is a bone inflammatory disease characterized by bone remodelling failure. The detailed mechanism of bone erosion in OM is still unclear. Previous studies have reported that bacteria directly mediate bone destruction by inducing osteoblast apoptosis in vitro [44]. Moreover, osteoclasts were stimulated with surface-associated material in an *S. aureus*-infected murine model [45,46]. However, we believe that the mechanism of bone destruction associated with osteomyelitis cannot be explained solely by one factor, such as the enhanced bone resorption ability of osteoclasts or the weakened osteogenic ability of osteoblasts. We speculate that this is due to the imbalance of the bone remodelling process caused by the damage of the reversal phase, resulting in bone destruction.

Our study preliminarily explored the potential role of OSCs in bone remodelling. However, our research has several limitations. (1) We collected and dissociated only five cortical bone samples, including two normal, two infected, and one reconstructed sample, resulting in a relatively small overall sample size. This may not adequately represent the state of cells during bone remodelling under different pathological conditions. (2) We need to further characterize OSCs in more detail, including identifying the cytokines that mediate their high chemotactic ability through sorting these living cells by specific surface markers or constructing IDO1-2A-EGFP fluorescence-labelled mice in the future. (3) There is only a causal correlation between the OSC and the fracture healing process. Currently, we are afraid that we cannot investigate the direct role of the OSC in bone remodelling. We have not identified the key regulators of OSCs, which could be helpful for evaluating the role of

OSCs in bone remodelling by performing gain/loss assays *in vivo*. After using ATAC-seq, CUT-Tag-seq and RNA-seq assays to identify key transcription factors of OSCs, we can further investigate the specific roles of OSCs by regulating the expression of key regulators. (4) Pseudotime analysis of the osteoclast lineage indicated that the timing of the differentiation of OSC cells was positioned between macrophages and osteoclast precursors. Normally, inducing osteoclast precursors requires 4–5 days. Therefore, we refined the induction period and compared the expression levels of genes characteristic of OSCs after 1, 2, 3, 4, 6, and 8 days of osteoclast induction to estimate the approximate time point at which OSC cells appeared. However, 72 h was not an exact induction time for OSC cells but should be an approximate time deduced from the peak expression of genes such as *IDO1*, *CCL3* and *CCL4*.

Based on these findings, we propose a novel bone remodelling hypothesis (Fig. 5). Monocyte-derived macrophages, primarily OSCs, stably reside in cortical bone (Fig. 7). When bone remodelling is initiated, OSCs can recruit many osteoprogenitor cells to the site of reconstruction (Fig. 7). OSCs themselves can further differentiate into osteoclasts, facilitating bone resorption while simultaneously undergoing osteocytic coupling. As bone resorption is completed, the recruited osteoprogenitor cells can be induced by osteoclasts or osteomorph cells to differentiate into mature osteoblasts, thereby achieving a coordinated process of bone resorption and formation (Fig. 7). If the survival stage of OSCs in the bone remodelling microenvironment is shortened or restricted, osteoprogenitor cells cannot be effectively recruited to the site of reconstruction, leading to delayed or impaired bone repair (Fig. 7).

4. Conclusion

In this study, we created a comprehensive cell atlas that covers normal, infected, and reconstructed cortical bone. Within the osteoclast lineages, we identified a new subset, referred to as OSCs, in the early stage via trajectory pseudotime analysis. Subsequently, we confirmed the presence of OSCs, which displayed the highest chemotactic activity among all lineage subsets. We revealed the significant role of cells in the early stage of the osteoclast lineage in recruiting MSCs. Our data suggest that OSCs may have a positive correlation with the presence of bone MSCs and their contribution to bone remodelling. These findings offer new insights and insights for understanding bone reversal-related diseases and may serve as novel therapeutic targets for conditions such as bone infection and delayed bone healing.

Ethical approval and consent to participate

Study has been approved by the Army Medical University First Affiliated Hospital Ethics Committee ((A)KY2021084). No individual personal data is included in the study. All patients provided necessary consent to participate in this study, including consent to participate in the study where appropriate.

Consent for publication

All authors have approved of the consents of this manuscript and provided consent for publication.

Availability of data and materials

The scRNA-seq data have been deposited in the Genome Sequence Archive for Humans (PRJCA007252). Human femoral head scRNA-seq data were obtained from the GEO database and GSA (GSE169396). All other relevant data from this study are available from the corresponding authors upon reasonable request.

Competing interests

The authors declare no conflicts of interest.

Funding

The authors thank all the colleagues for their helpful and valuable discussions. This study was supported by grants from the National Natural Science Foundation of China (No. 81672160) and the National Science Fund for Young Scholars of China (No. 8220091332). This study was partially supported by the University Grants Committee, Research Grants Council of Hong Kong, China (14113723, N_CUHK472/22, T13-402/17-N and AoE/M-402/20).

Acknowledgements

All persons who have made substantial contributions to the work reported in the manuscript (e.g., technical help, writing and editing assistance, general support), but who do not meet the criteria for authorship, are named in the Acknowledgements and have given us their written permission to be named. If we have not included an Acknowledgements, then that indicates that we have not received substantial contributions from non-authors.

Appendix A. Supplementary data

Supplementary data to this article can be found online at <https://doi.org/10.1016/j.jot.2024.06.010>.

References

- [1] Hadjidakis DJ, Androulakis II. Bone remodeling. *Ann N Y Acad Sci* 2006;1092:385–96.
- [2] Katsimbri P. The biology of normal bone remodelling. *Eur J Cancer Care* 2017;26(6).
- [3] Cui J, Shibata Y, Zhu T, Zhou J, Zhang J. Osteocytes in bone aging: advances, challenges, and future perspectives. *Ageing Res Rev* 2022;77:101608.
- [4] Mosekilde L. Consequences of the remodelling process for vertebral trabecular bone structure: a scanning electron microscopy study (uncoupling of unloaded structures). *Bone Miner* 1990;10(1):13–35.
- [5] Makris GP, Saffar JL. Disturbances in bone remodeling during the progress of hamster periodontitis. A morphological and quantitative study. *J Periodontol Res* 1985;20(4):411–20.
- [6] Compston J. Glucocorticoid-induced osteoporosis: an update. *Endocrine* 2018;61(1):7–16.
- [7] Baldi S, Becorpi A. Prevention, diagnosis and treatment of osteoporosis following menopause induced due to oncological disease. *Clin Cases Miner Bone Metab* 2009;6(3):261–3.
- [8] Bolamperti S, Villa I, Rubinacci A. Bone remodeling: an operational process ensuring survival and bone mechanical competence. *Bone Res* 2022;10(1):48.
- [9] Tran, Van P, Vignery A, Baron R. An electron-microscopic study of the bone-remodeling sequence in the rat. *Cell Tissue Res* 1982;225(2):283–92.
- [10] Everts V, Delaisse JM, Korper W, Jansen DC, Tigchelaar-Gutter W, Saftig P, et al. The bone lining cell: its role in cleaning Howship's lacunae and initiating bone formation. *J Bone Miner Res* 2002;17(1):77–90.
- [11] Heinemann DE, Siggelkow H, Ponce LM, Viereck V, Wiese KG, Peters JH. Alkaline phosphatase expression during monocyte differentiation. Overlapping markers as a link between monocytic cells, dendritic cells, osteoclasts and osteoblasts. *Immunobiology* 2000;202(1):68–81.
- [12] Li L, Xiong F, Wang Y, Zhang S, Gong Z, Li X, et al. What are the applications of single-cell RNA sequencing in cancer research: a systematic review. *J Exp Clin Cancer Res* : CR 2021;40(1):163.
- [13] Stuart T, Butler A, Hoffman P, Hafemeister C, Papalexi E, Mauck 3rd WM, et al. Comprehensive integration of single-cell data. *Cell* 2019;177(7):1888–1902 e21.
- [14] van der Maaten L, Hinton G. Visualizing Data using t-SNE. *J Mach Learn Res* 2008;9:2579–605 [English].
- [15] Trapnell C, Cacchiarelli D, Grimsby J, Pokharel P, Li S, Morse M, et al. The dynamics and regulators of cell fate decisions are revealed by pseudotemporal ordering of single cells. *Nat Biotechnol* 2014;32(4):381–6.
- [16] Satija R, Farrell JA, Gennert D, Schier AF, Regev A. Spatial reconstruction of single-cell gene expression data. *Nat Biotechnol* 2015;33(5):495–502.
- [17] Filipowska J, Tomaszewski KA, Niedzwiedzki L, Walocha JA, Niedzwiedzki T. The role of vasculature in bone development, regeneration and proper systemic functioning. *Angiogenesis* 2017;20(3):291–302.
- [18] Marenzana M, Arnett TR. The key role of the blood supply to bone. *Bone Res* 2013;1(3):203–15.
- [19] Ray K. Bone: the immune system takes control of bone homeostasis. *Nat Rev Rheumatol* 2014;10(7):382.
- [20] Boyle WJ, Simonet WS, Lacey DL. Osteoclast differentiation and activation. *Nature* 2003;423(6937):337–42.

- [21] McDonald MM, Khoo WH, Ng PY, Xiao Y, Zamerli J, Thatcher P, et al. Osteoclasts recycle via osteomorphs during RANKL-stimulated bone resorption. *Cell* 2021;184(5):1330–1347 e13.
- [22] Kukita T, Nakao J, Hamada F, Kukita A, Inai T, Kurisu K, et al. Recombinant LD78 protein, a member of the small cytokine family, enhances osteoclast differentiation in rat bone marrow culture system. *Bone Miner* 1992;19(3):215–23.
- [23] Scheven BA, Milne JS, Hunter I, Robins SP. Macrophage-inflammatory protein-1alpha regulates preosteoclast differentiation in vitro. *Biochem Biophys Res Commun* 1999;254(3):773–8.
- [24] Ikeda K, Takeshita S. The role of osteoclast differentiation and function in skeletal homeostasis. *J Biochem* 2016;159(1):1–8.
- [25] Eriksen EF. Cellular mechanisms of bone remodeling. *Rev Endocr Metab Disord* 2010;11(4):219–27.
- [26] Qiu X, Liu Y, Shen H, Wang Z, Gong Y, Yang J, et al. Single-cell RNA sequencing of human femoral head in vivo. *Aging (Albany NY)* 2021;13(11):15595–619.
- [27] Wang L, You X, Zhang L, Zhang C, Zou W. Mechanical regulation of bone remodeling. *Bone Res* 2022;10(1):16.
- [28] Pajarinen J, Lin T, Gibon E, Kohno Y, Maruyama M, Nathan K, et al. Mesenchymal stem cell-macrophage crosstalk and bone healing. *Biomaterials* 2019;196:80–9.
- [29] Batoon L, Millard SM, Wullschlegel ME, Preda C, Wu AC, Kaur S, et al. CD169(+) macrophages are critical for osteoblast maintenance and promote intramembranous and endochondral ossification during bone repair. *Biomaterials* 2019;196:51–66.
- [30] Sinder BP, Pettit AR, McCauley LK. Macrophages: their emerging roles in bone. *J Bone Miner Res* 2015;30(12):2140–9.
- [31] Chang MK, Raggatt LJ, Alexander KA, Kuliwaba JS, Fazzalari NL, Schroder K, et al. Osteal tissue macrophages are intercalated throughout human and mouse bone lining tissues and regulate osteoblast function in vitro and in vivo. *J Immunol* 2008;181(2):1232–44.
- [32] Wu AC, Raggatt LJ, Alexander KA, Pettit AR. Unraveling macrophage contributions to bone repair. *BoneKey Rep* 2013;2:373.
- [33] Ma Q, Liang M, Wu Y, Dou C, Xu J, Dong S, et al. Small extracellular vesicles deliver osteolytic effectors and mediate cancer-induced osteolysis in bone metastatic niche. *J Extracell Vesicles* 2021;10(4):e12068.
- [34] Delaisse JM, Andersen TL, Kristensen HB, Jensen PR, Andreasen CM, Soe K. Re-thinking the bone remodeling cycle mechanism and the origin of bone loss. *Bone* 2020;141:115628.
- [35] Soesatyo M, Biewenga J, Kraal G, Sminia T. The localization of macrophage subsets and dendritic cells in the gastrointestinal tract of the mouse with special reference to the presence of high endothelial venules. An immuno- and enzyme-histochemical study. *Cell Tissue Res* 1990;259(3):587–93.
- [36] Xu J, Wu HF, Ang ES, Yip K, Woloszyn M, Zheng MH, et al. NF-kappaB modulators in osteolytic bone diseases. *Cytokine Growth Factor Rev* 2009;20(1):7–17.
- [37] Riggs BL, Parfitt AM. Drugs used to treat osteoporosis: the critical need for a uniform nomenclature based on their action on bone remodeling. *J Bone Miner Res* 2005;20(2):177–84.
- [38] Chen X, Wang Z, Duan N, Zhu G, Schwarz EM, Xie C. Osteoblast-osteoclast interactions. *Connect Tissue Res* 2018;59(2):99–107.
- [39] Sims NA, Martin TJ. Osteoclasts provide coupling signals to osteoblast lineage cells through multiple mechanisms. *Annu Rev Physiol* 2020;82:507–29.
- [40] Tang Y, Wu X, Lei W, Pang L, Wan C, Shi Z, et al. TGF-beta1-induced migration of bone mesenchymal stem cells couples bone resorption with formation. *Nat Med* 2009;15(7):757–65.
- [41] Martin TJ, Sims NA. Osteoclast-derived activity in the coupling of bone formation to resorption. *Trends Mol Med* 2005;11(2):76–81.
- [42] Pederson L, Ruan M, Westendorf JJ, Khosla S, Oursler MJ. Regulation of bone formation by osteoclasts involves Wnt/BMP signaling and the chemokine sphingosine-1-phosphate. *Proc Natl Acad Sci U S A* 2008;105(52):20764–9.
- [43] Zhao C, Irie N, Takada Y, Shimoda K, Miyamoto T, Nishiwaki T, et al. Bidirectional ephrinB2-EphB4 signaling controls bone homeostasis. *Cell Metabol* 2006;4(2):111–21.
- [44] Alexander EH, Bento JL, Hughes Jr FM, Marriott I, Hudson MC, Bost KL. Staphylococcus aureus and Salmonella enterica serovar Dublin induce tumor necrosis factor-related apoptosis-inducing ligand expression by normal mouse and human osteoblasts. *Infect Immun* 2001;69(3):1581–6.
- [45] Lau YS, Wang W, Sabokbar A, Simpson H, Nair S, Henderson B, et al. Staphylococcus aureus capsular material promotes osteoclast formation. *Injury* 2006;37(Suppl 2):S41–8.
- [46] Nair S, Song Y, Meghji S, Reddi K, Harris M, Ross A, et al. Surface-associated proteins from Staphylococcus aureus demonstrate potent bone resorbing activity. *J Bone Miner Res* 1995;10(5):726–34.